Finding activation pathway of coupled displacive-diffusional defect processes in atomistics: Dislocation climb in fcc copper

Sanket Sarkar,[1] Ju Li,[2,*] William T. Cox,[1] Erik Bitzek,[3] Thomas J. Lenosky,[2] and Yunzhi Wang[1,†]

[1]*Department of Materials Science and Engineering, The Ohio State University, Columbus, Ohio 43210, USA*

[2]*Department of Nuclear Science and Engineering and Department of Materials Science and Engineering, Massachusetts Institute of Technology, Cambridge, Massachusetts 02139, USA*

[3]*Department Werkstoffwissenschaften, Universität Erlangen-Nürnberg, 91058 Erlangen, Germany*

(Received 16 June 2011; revised manuscript received 5 July 2012; published 30 July 2012)

The majority of solid-state deformation and transformation processes involve coupled displacive-diffusional mechanisms, of which a detailed atomic picture does not exist. We present here a complete atomistic description of one such process by which an extended edge dislocation in face-centered-cubic (fcc) metals may climb at finite temperature under supersaturation of vacancies. We employ an approach called "diffusive molecular dynamics," which can capture the diffusional time scale while maintaining atomic resolution by coarse graining over atomic vibrations and evolving atomic density clouds. We find that, unlike the Thomson-Balluffi mechanism, if simultaneous displacive and diffusive events are allowed, a coupled displacive-diffusional pathway exists for extended double jog formation. Along this pathway, the activation energy is lower than the previous theoretical predictions and on par with the experimental observations.

DOI: 10.1103/PhysRevB.86.014115 PACS number(s): 61.72.Cc, 02.70.Ns, 61.72.Bb, 66.30.−h

I. INTRODUCTION

In most solid-state processes, the coupled displacive-diffusional mechanism is the rule rather than an exception. For example, structural phase transformations often involve coupled lattice shear, shuffle, and diffusion.[1] Curvature-driven grain growth may involve coupled tangential (displacive) and normal (diffusional) migration of grain boundaries.[2] Creep deformation, the focus of the present study, involves both displacive (conservative) and diffusional (nonconservative) motion of dislocations.[3] It is generally accepted that power-law creep, where steady-state creep strain rate $\dot{\epsilon}$ is proportional to a power of the applied stress σ ($\dot{\epsilon} \propto \sigma^n$), is a result of these coupled diffusive-displacive motions.[4,5] In pure metals and some alloys, where $n \geqslant 4.5$, the creep rate is believed to be governed primarily by the climb of edge dislocations.[6] Because of time scale limitations, conventional molecular dynamics (MD) has been applied to study mostly dislocation glide in the past thirty years; atomistic modeling of climb has always been a challenging task.[7] Here, we employ a method called "diffusive molecular dynamics" (DMD)[8] that evolves $5N$ degrees of freedom: $\{\mathbf{X}_i, \alpha_i, c_i\}$, which are the mean position, the Gaussian width, and the occupation probability or concentration, respectively, of N atomic density clouds. Developed in the grand canonical ensemble, DMD is a chemical and kinetic extension of the variational Gaussian (VG) method,[9,10] which coarse grains over atomic vibrations but, unlike VG, allows for simultaneous displacive and mass-action dynamics such as lattice diffusion.

Climb of an edge dislocation should occur via climb of individual jogs. This scenario becomes complicated when dislocations are dissociated (extended)—a natural occurrence in face-centered-cubic (fcc) metals. Stroh proposed a mechanism[11] that requires the glissile constriction of the two partial dislocations, hereafter referred to as partials, as a precursor for the climb of an extended dislocation. In an illustration of the reaction coordinates, Fig. 1, Stroh's path involves glissile action first, followed by nonconservative mass action. But mechanisms in the reverse order have also been suggested.[12–14] Thomson and Balluffi[13] proposed that the first step of climb involves diffusive aggregation of a prismatic loop on one of the partials. In contrast to the Stroh path, the Thomson-Balluffi (TB) path requires nonconservative aggregation first, followed by conservative glissile dissociation of the prismatic loop. Grilhé *et al.*[15,16] have computed, based on continuum elasticity theory, that there exists a critical size n_C of the TB prismatic loop (blue circle in Fig. 1) above which the pure glissile dissociation of the prismatic loop becomes monotonically downhill in energy; otherwise, the activation energy for purely glissile formation of dissociated double jogs, seen experimentally,[13,17,18] is quite large ($\sim 10^1$ eV). Here, using the DMD method,[8] we demonstrate that a smaller n_C is possible along the TB path by relieving the constraint of purely glissile relaxation: DMD shows that $n_C \sim 3$ is sufficient to trigger a monotonically downhill path in the grand potential, along a coupled diffusive-displacive reaction coordinate as illustrated in Fig. 1. The coarse-grained activation barrier for this process is only ∼0.83 eV, on top of a lattice diffusion barrier of ∼0.7 eV. Thus, our calculation is on par with experimental observations that double-jog nucleation is an easy process even on widely extended dislocations under moderate to high driving forces.[3,19,20]

II. METHODOLOGY

A. Diffusive molecular dynamics

The DMD method is described in Ref. 8. Here, it may suffice to say that compared to $6N$ variables in MD, the atomic positions and the momenta $\{\mathbf{x}_i, \mathbf{p}_i\}$, for $i = 1 \ldots N$, N being the number of atoms, DMD has $5N$ degrees of freedom: $\{\mathbf{X}_i, \alpha_i, c_i\}$, which are the mean position, the Gaussian width, and the site-occupation probability or concentration, respectively, of atomic density clouds. The Helmholtz free energy of the system, F_{DMD}, is expressed in terms of $\{\mathbf{X}_i, \alpha_i, c_i\}$

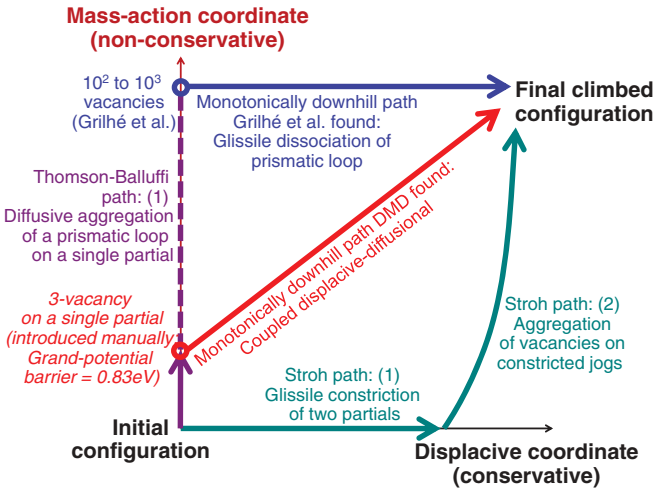

FIG. 1. (Color online) Schematic representation of the proposed climb processes in the reaction coordinate space.

as

$$F_{\mathrm{DMD}} = \frac{1}{2}\sum_{i=1}^{N}\sum_{j\neq i} c_i c_j w(X_{ij},\alpha_{ij}) + \sum_{i=1}^{N} c_i E(\overline{\psi}_i) + \frac{d}{2}k_{\mathrm{B}}T\sum_{i=1}^{N} c_i\left\{\ln\left[\frac{\alpha_i\Lambda_T^2}{\pi}\right]-1\right\} + k_{\mathrm{B}}T\sum_{i=1}^{N}\{c_i\ln c_i + (1-c_i)\ln(1-c_i)\}, \quad (1)$$

where

$$\overline{\psi}_i = \sum_{j\neq i} c_j\psi(X_{ij},\alpha_{ij}), \quad X_{ij} = |\mathbf{X}_{ij}| = |\mathbf{X}_i - \mathbf{X}_j|,$$
$$\alpha_{ij} = \left(\alpha_i^{-1} + \alpha_j^{-1}\right)^{-1},$$

and $\Lambda_T = \hbar\sqrt{2\pi/mk_{\mathrm{B}}T}$ is the de Broglie thermal wavelength, k_{B} is the Boltzmann constant, T is the absolute temperature, m is the atomic mass, and d is the dimensionality of the system. In the above expression, E is the embedding function, w is the Gaussian-averaged pair potential u, and ψ is the Gaussian-averaged density function ρ of an embedded atom method (EAM) potential

$$E_{\mathrm{tot}} = \sum_{i=1}^{N} E(\overline{\rho}_i) + \frac{1}{2}\sum_{i=1}^{N}\sum_{j\neq i} u(x_{ij}), \quad (2)$$

where $\overline{\rho}_i = \sum_{j\neq i}\rho(x_{ij})$. An exchange chemical potential between an atom and a vacancy for site i is defined as

$$\mu_i \equiv \left.\frac{\partial F_{\mathrm{DMD}}(\{\mathbf{X}_i,\alpha_i,c_i\})}{\partial c_i}\right|_{\{\mathbf{X}_i,\alpha_i\}}. \quad (3)$$

Once the sitewise exchange chemical potential is defined, a general master equation[21] for diffusion can be invoked on a network of moving atomic sites.

The VG method was extended in the grand canonical ensemble earlier by Phillpot[10] in the context of simulated quenching technique,[22,23] but the resulting free energy does not include the configurational entropy term ($k_{\mathrm{B}}T[c\ln c + (1-c)\ln(1-c)]$) and is coupled with an ansatz Lagrangian to describe the dynamics of a system. On the other hand, the purely relaxational part of the DMD can be conceptually and formalistically regarded as solving the Cahn-Hilliard equation[1] on a "moving-atoms grid," taking the regular-solution chemical free energy model with long-range elastic interactions, short-range coordination interaction, and gradient thermodynamics all automatically included.

During a DMD simulation, each time step is realized in two parts. First, the variables $\{\mathbf{X}_i,\alpha_i\}$ are statically minimized holding $\{c_i\}$ constant. This process of establishing mechanical and vibrational equilibrium is instantaneous because $\{\mathbf{X}_i\}$ and $\{\alpha_i\}$ change on the inertial (ps) and thermalization (100 ps) time scales, respectively, both of which are much smaller than the diffusional time scale determined by $\tau = r_0^2/4\pi D_{\mathrm{V}}$, where r_0 is the nearest neighbor distance and D_{V} is the vacancy diffusivity. Then in the second part, the $\{c_i\}$ are integrated numerically according to the chemical potential differences, holding $\{\mathbf{X}_i,\alpha_i\}$ constant, in order to approach chemical equilibrium gradually. Because displacive relaxation of $\{\mathbf{X}_i,\alpha_i\}$ is "instantaneous" in DMD, the fundamental "clock" of DMD is controlled by the value of chemical diffusivity, not by atomic vibration. The DMD algorithm has been embedded in the LAMMPS molecular dynamics code[24] by creating a new atom type, enabling us to use its vast resources and parallelization. A Gaussian-averaged Cu embedded-atom method potential[8] was used to represent the pairwise interactions and electron density in copper for this study. We report time in terms of (dimensionless) reduced time $\tilde{t} \equiv t/\tau$, t being the simulated time.

For the calculation of stress tensor, with $\{\alpha_i\}$ instantaneously minimized for an arbitrary $\{\mathbf{X}_i,c_i\}$ configuration, it can be shown that the virial stress formula can be applied to just the first two terms of F_{DMD} to calculate the stress tensor in DMD, as if it were the normal interatomic potential in MD with $\mathbf{X}_i$ replaced by $\mathbf{x}_i$, and pretending $\{\alpha_i,c_i\}$ are frozen parameters. So, the atomic level stress for site i in DMD is expressed as

$$\boldsymbol{\sigma}_i = \frac{1}{2\overline{\omega}}\sum_{j\neq i}\mathbf{X}_{ij}\otimes\frac{\partial F_{\mathrm{DMD}}(\{\mathbf{X}_i,\alpha_i,c_i\})}{\partial\mathbf{X}_{ij}}, \quad (4)$$

where $\overline{\omega}$ represents the average atomic volume, and $\mathbf{X}_{ij} = \mathbf{X}_i - \mathbf{X}_j$.

B. The nudged elastic band method on DMD free energy

The variables $\{\mathbf{X}_i,\alpha_i,c_i\}$, $i = 1\ldots N$, N being the total number of sites in the system, define a $5N$ dimensional configuration space in DMD. In order to explore the free energy surface in the grand canonical ensemble, one must consider the DMD system in contact with an infinitely large reservoir with which the system is in equilibrium and can exchange mass. Then the appropriate potential to feed into the nudged elastic band (NEB) "machinery" is the grand potential Ω_{DMD},[25] defined as

$$\Omega_{\mathrm{DMD}}(\mu,V,T) = F_{\mathrm{DMD}}(N,V,T) - \mu_0\sum_{i=1}^{N} c_i, \quad (5)$$

where μ_0 is the constant chemical potential of the reservoir. Ω_{DMD} represents the Legendre-transformed free energy that accounts for the penalty in any change in the total mass ($\sum_i c_i$) of the system.

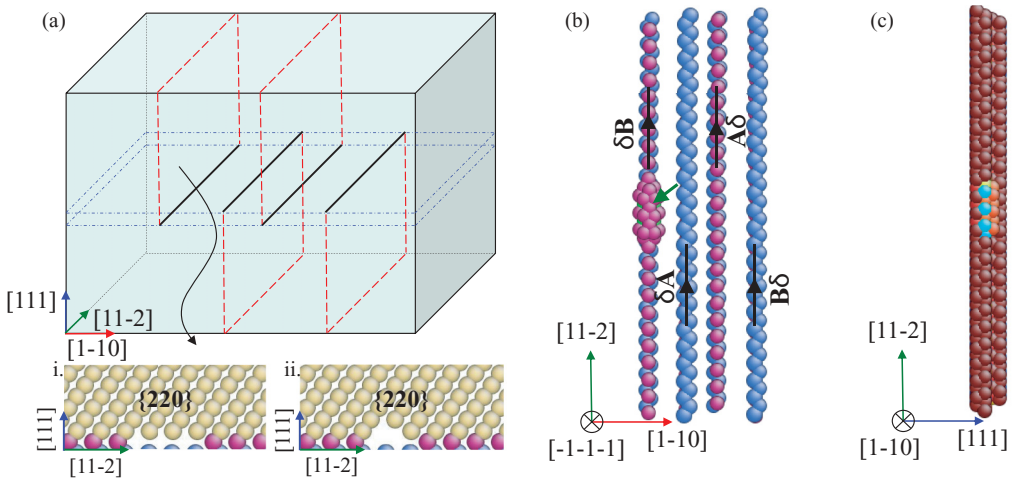

FIG. 2. (Color online) Initial configuration at $\tilde{t} = 0$. (a) A schematic representation of the simulation cell showing the locations of the {220} extra half planes corresponding to the partials. In the inset, two different ways of introducing the "3-vacancy roughness" on {220} are shown. (b) ⟨111⟩ view of the dislocation lines by coordination plot. Only the non-perfectly-coordinated ($\neq$12) sites are shown. The partial $\boldsymbol{\delta}\mathbf{B}$ on the left shows the 3-vacancy roughness indicated by the oblique green arrow. The Burgers vectors are mentioned as per Thompson's notation, and the line directions are shown by black arrows. (c) $\langle 1\bar{1}0\rangle$ view of the centrosymmetry plot of the initial configuration showing that the dipoles are $2d_{111}$ apart. For coordination calculation, sites having $\bar{c} \leqslant 0.01$ were excluded from the nearest-neighbor calculation.

In the NEB method,[26–28] an elastic band with $K+1$ replicas or nodes, denoted as $[\mathbf{R}_0, \mathbf{R}_1, \mathbf{R}_2, \ldots, \mathbf{R}_K]$, where $\mathbf{R}_0$ and $\mathbf{R}_K$ correspond to the initial and the final replicas, is considered. In this case, each replica represents a point in the $5N$ dimensional configuration space spanned by $\{\mathbf{X}_i, \alpha_i, c_i\}$, $i = 1 \ldots N$. The total force acting on any replica is calculated as the vector sum of the spring force along the local tangent and the true force perpendicular to the local tangent, expressed as

$$\mathbf{F}_j = \mathbf{F}_j^s\big|_{||} + \mathbf{F}_j^p\big|_{\perp}, j = 0 \ldots K. \tag{6}$$

The subscripts $||$ and $\perp$ stand for the parallel and the perpendicular component of the forces resolved on the local tangent to the node. The true force $\mathbf{F}_j^p$, in the context of DMD, is calculated as

$$\mathbf{F}_j^p = \left\{ \frac{\partial \Omega_{\mathrm{DMD}}}{\partial \mathbf{X}}, \frac{\partial \Omega_{\mathrm{DMD}}}{\partial \alpha}, \mu - \mu_0 \right\}. \tag{7}$$

The spring force is an artificial force that depends on the interreplica distances $|\mathbf{R}_j - \mathbf{R}_{j+1}|$, as[26]

$$\mathbf{F}_j^s|_{||} = \mathbf{k}_{\mathrm{dof}}(|\mathbf{R}_{j+1} - \mathbf{R}_j| - |\mathbf{R}_j - \mathbf{R}_{j-1}|)\hat{\boldsymbol{\tau}}_j, \tag{8}$$

where $\mathbf{k}_{\mathrm{dof}}$ is the spring constant vector with each component corresponding to a particular type of degrees of freedom. In calculating $\hat{\boldsymbol{\tau}}_j$, the normalized local tangent on image j, an improved tangent calculation as per Henkelman and Jónsson[26] is adopted to avoid the formation of kinks on the minimum energy pathway (MEP). The initial chain of states is created by linearly interpolating the two end images. After that, the replicas are relaxed according to the damped dynamics FIRE (fast inertial relaxation engine)[29] subject to the force field $\mathbf{F}_j$ until the chain converges to the MEP. During the relaxation, the forces on each replica are simultaneously updated as well. Convergence is ascertained when there is no change in the MEP and the maximum force on any replica is less than a prescribed tolerance.

III. MODEL SETUP

To study the climb process, a copper crystal of dimension $L_x = 15.09$ nm, $L_y = 10.62$ nm, and $L_z = 12.52$ nm, spanned by fcc lattice vectors $\mathbf{u_x} = [1\bar{1}0]$, $\mathbf{u_y} = [11\bar{2}]$, $\mathbf{u_z} = [111]$, was created [Fig. 2(a)].[30] The cell contained approximately $N = 170\,000$ atoms with an edge dislocation dipole inside, whose Burgers vectors were $\pm\frac{a}{2}[1\bar{1}0]$, parallel (or antiparallel) to $\mathbf{u_x}$, a being the lattice parameter. The dislocation lines were oriented along $\mathbf{u_y}$ with the sense vector $\boldsymbol{\xi}$ taken as $\boldsymbol{\xi} = \mathbf{u_y}/|\mathbf{u_y}|$. The two edge dislocations that were two glide planes ($2d_{111}$) apart were introduced in the same manner as Rodney and Martin's,[31] where the atoms were displaced in the x and z directions according to the isotropic elasticity solution for the displacement field of the dislocations.[3] Such narrow dipole configuration was chosen because in that limit any elasticity description fails, eliminating applicability of many other methods, such as kinetic Monte Carlo. The system was then MD static relaxed at 0 K in an *NPT* ensemble using the LAMMPS molecular dynamics code[24] under periodic boundary conditions (PBC) in all three directions and zero applied stress. After the relaxation, the top (≡positive edge $\perp$) and the bottom edge dislocation dissociated into Shockley partials according to $\mathbf{AB} = \mathbf{A}\boldsymbol{\delta} + \boldsymbol{\delta}\mathbf{B}$ and $\mathbf{BA} = \mathbf{B}\boldsymbol{\delta} + \boldsymbol{\delta}\mathbf{A}$, respectively (Thompson tetrahedron notation adopted), as shown in Figs. 2(a) and 2(b), and the dissociation width was found to be 1.82 nm, the cores being located by means of coordination number plot. This configuration was subsequently taken to 1200 K using equilibrium lattice parameter and equilibrium $\{\alpha_i\}$ for copper at this temperature[8] and was subjected to a constant 0.5% uniaxial compressive strain [∼950 MPa, volume averaged virial in Eq. (4)] in the $\mathbf{u_x}$ direction.

At 1200 K, our model predicts an equilibrium vacancy concentration of 6.2×10^{-6} corresponding to the vacancy formation (free) energy of $E_V^f = 1.24$ eV. However, by set-

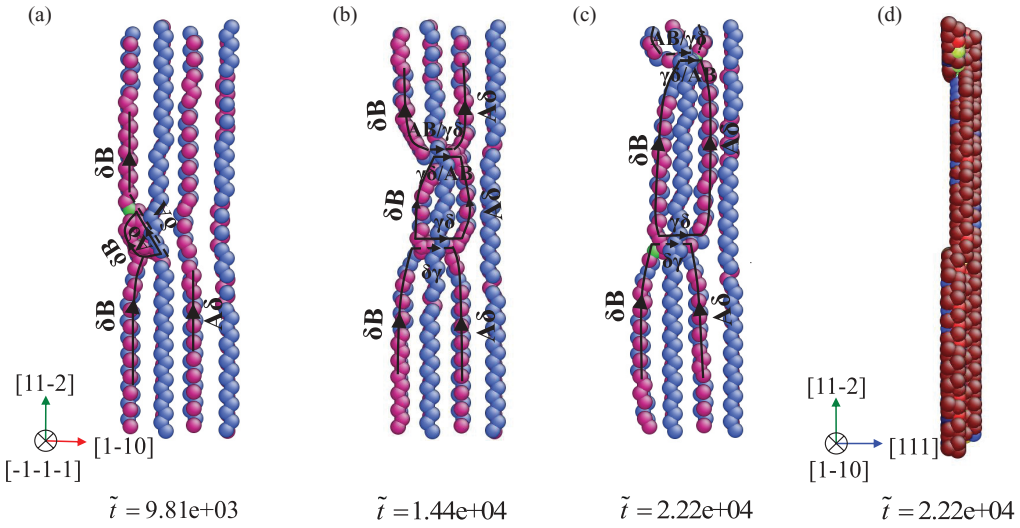

FIG. 3. (Color online) (a) Climb of the small stacking fault region by nucleation of prismatic loop **AB** followed by its growth and reaction with the partial $\boldsymbol{\delta B}$ at $\tilde{t} = 9.81 \times 10^3$. (b) Dislocation structure showing the double jog on the extended dislocations at $\tilde{t} = 1.44 \times 10^4$. (c) One jog swept across almost half of the line at $\tilde{t} = 2.22 \times 10^4$. (d) $[1\bar{1}0]$ view of the centrosymmetry plot of the same configuration showing climb by one atomic layer.

ting $c_i = 0.999$ for all sites, a higher background vacancy concentration of 10^{-3} was assumed. This supersaturation of point defects is observed in many climb environments such as irradiation damage and severe plastic deformation, and can exceed the equilibrium value by at least four orders of magnitude.[32,33] In our system, L_x and L_z determine the total dislocation density ρ_d by controlling the inter-dislocation spacing under PBC. Taking $L \approx 15.0$ nm, ρ_d can be anywhere between 10^{15} m^{-2} to 10^{16} m^{-2}, a dislocation density that is typically observed in heavily deformed metals.[34] Thus, a supersaturation of two to three orders of magnitude for this temperature was realistic for such deformed metals. Additionally, a thick layer of sites ($\sim$1.6 nm) at the supercell boundary in the $\pm\mathbf{u_z}$ direction were held at fixed concentration $c_i = 0.999$ to serve as far-field vacancy sources or sinks that correspond to, in reality, grain boundaries in bulk, etc. This maintained a steady supersaturation realized under applied stress and temperature.[35] We report our simulation results in terms of dimensionless time $\tilde{t}$, as described above.

IV. RESULTS AND DISCUSSION

Due to omission of the noise term in the master equation,[8] kinetics in DMD is only downhill and therefore it cannot capture uphill phenomena in the mass-action space. Hence, to overcome the critical activation energy corresponding to the nucleation of a loop on a partial, a "3-vacancy roughness" was created on a randomly chosen partial (here $\boldsymbol{\delta B}$) by reassigning $c_i = 0.001$ to three sites in a row at the end of the extra half plane {220} as shown in the inset of Fig. 2(a.i) and Fig. 2(b). This was motivated from the realization that at atomic level, the process of climb is initiated by binding a vacancy to the core (Ref. 3, p. 583, and Ref. 36). We note that there are two ways of introducing a three-vacancy jog on a {220} half plane, as shown in the inset of Fig. 2(a). On collapsing by energy minimization, this 3-vacancy roughness formed a vacancy-type prismatic loop **AB** on the partial $\boldsymbol{\delta B}$ (Ref. 3, p. 583) as shown in Fig. 4(b). We refrained from introducing multiple nucleation events so that the current study remains focused on "probing" the energy landscape in the coupled displacive-diffusional reaction coordinate space.[7]

Since a DMD system is typically an open system, we track the grand potential Ω_{DMD} of the system as defined in Eq. (5). The chemical potential of the reservoir, μ_0, was estimated to be -4.52 eV for the present case, calculated by subjecting the reservoir to the same thermodynamic boundary conditions (here the same background vacancy concentration, strain, and temperature) as the system. To show that the configuration with the 3-vacancy roughness was past the activation barrier, Ω_{DMD} was calculated for all four configurations—the *0-vacancy* ($\equiv$all sites assigned $c_i = 0.999$ uniformly), the *1-vacancy* ($\equiv$only one site at the end of the extra half plane reassigned to $c_i = 0.001$), the *2-vacancy* ($\equiv$two sites in a row reassigned to $c_i = 0.001$), and the 3-vacancy configurations—by relaxing $\{\mathbf{X}_i, \alpha_i\}$ statically under the applied strain. Referenced to the grand potential for the 0-vacancy case, $\Omega_{\mathrm{DMD}}^{0\mathrm{vac}}$, those for the 1-vacancy, 2-vacancy, and 3-vacancy configurations were found to be 0.52 eV (or $5.0 k_{\mathrm{B}}T$), 0.83 eV (or $8.1 k_{\mathrm{B}}T$), and 0.80 eV (or $7.7 k_{\mathrm{B}}T$), respectively. This activation energy barrier of $<$1 eV is significantly lower than any previous theoretical estimate.[15]

Under the uniaxial compression of 0.5%, as the system started evolving, the 3-vacancy roughness underwent a transformation where one of the end vacant sites was filled up at the cost of one site on the adjacent $[1\bar{1}0]$ plane, resulting in the formation of a zigzag trivacancy configuration. A similar observation was noted for the configuration in Fig. 2(a.ii) at 0.7% strain, where the topmost vacant site was filled instead. After that, one leg of the zigzag structure started attracting more vacancies forming a row of close-packed vacancies, which resulted in enlargement of the prismatic loop **AB**, the **BA** part of which interacted with $\boldsymbol{\delta B}$ to form $\boldsymbol{\delta A}$ by the reaction

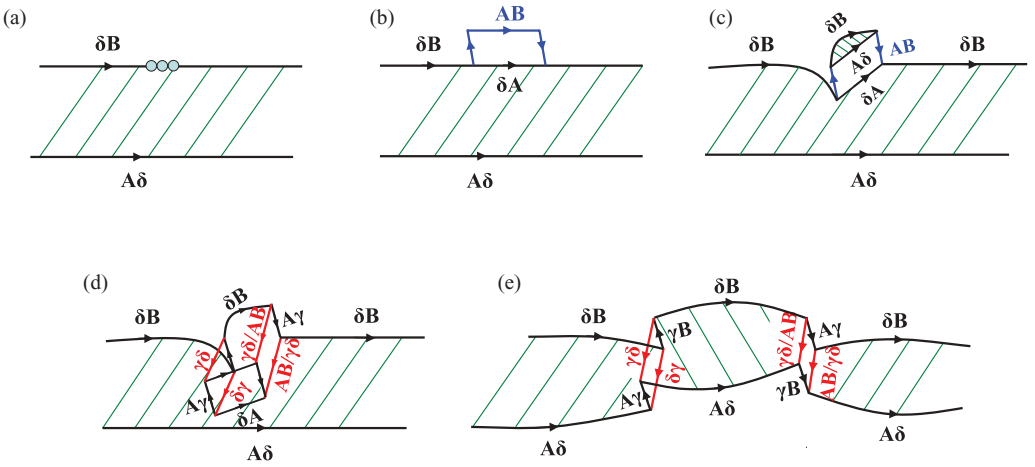

FIG. 4. (Color online) Climb mechanism for dissociated dislocations. (a) The initial edge dislocation **AB** dissociates into partials $\boldsymbol{\delta}$**B** and **A**$\boldsymbol{\delta}$. The shaded area shows the stacking fault ribbon. Three vacancies are bound to the core of $\boldsymbol{\delta}$**B**. (b) Prismatic loop **AB** nucleates on $\boldsymbol{\delta}$**B**. (c) **AB** again dissociates to form a partial $\boldsymbol{\delta}$**B** and a dipole **A**$\boldsymbol{\delta}$ − $\boldsymbol{\delta}$**A**. (d) Glide extension of the prismatic loop that happens after the prismatic loop attains some critical size. (e) Formation of the extended double jog.

$\boldsymbol{\delta}\mathbf{B} + \mathbf{BA} = \boldsymbol{\delta}\mathbf{A}$. The top part again dissociated by glide as $\mathbf{AB} = \mathbf{A}\boldsymbol{\delta} + \boldsymbol{\delta}\mathbf{B}$, creating a dipole $\mathbf{A}\boldsymbol{\delta} - \boldsymbol{\delta}\mathbf{A}$ and a partial $\boldsymbol{\delta}$**B** [Fig. 3(a) and Fig. 4(c)]. Until this point of the evolution, the process resulted in climb of a part of the stacking fault area bounded by curved partial $\boldsymbol{\delta}$**B** and straight partial **A**$\boldsymbol{\delta}$. The twisting of the dislocation line is reported and explained elsewhere[17] in terms of the osmotic force couple that acts on the loop jogs **AB**. This process continued until $\tilde{t} = 1.01 \times 10^4$, when the loop, containing five vacancies, was large enough so that it created a double jog on the extended dislocation by glide extension [Figs. 4(c)–4(e)]. The corresponding atomic structure at $\tilde{t} = 1.44 \times 10^4$ is shown in Fig. 3(b). This glide extension happened instantaneously in the DMD time scale. A schematic of this step drawn from the reaction of the Burgers vectors is shown in Fig. 4(d). During the evolution, the dislocation structure as a whole was found to glide in the $\pm\mathbf{u}_\mathbf{x}$ direction, and to relax accordingly in the surrounding stress field.

It can readily be observed in Fig. 3(b) that the partials **A**$\boldsymbol{\delta}$ and $\boldsymbol{\delta}$**B** showed different degrees of constriction for the two jogs, a phenomenon which has been reported by both simulation (MD static minimization)[31] and experiments.[37] The degree of constriction depends on the line tension of the stair-rod dislocations. Since $\boldsymbol{\gamma\delta}$-$\boldsymbol{\delta\gamma}$ Lomer-Cottrell segments have smaller Burgers vector than that of **AB**/$\boldsymbol{\gamma\delta}$-$\boldsymbol{\gamma\delta}$/**AB** stair rods, and consequently lower line tension, the jog corresponding to the former remained more extended. However, since the height of the jogs was only one interplanar spacing in this case, using elastic arguments to comment further on the details, e.g., the asymmetry of the dissociation width on either side of a jog, may be questionable. It was found that the jog corresponding to **AB**/$\boldsymbol{\gamma\delta}$ stair rods had higher chemical potential and therefore attracted more vacancies which resulted in its movement in the $\mathbf{u}_\mathbf{y}$ direction. Figure 3(c) shows an intermediate configuration at $\tilde{t} = 2.22 \times 10^4$ where almost half of the dislocation line had climbed. This is more evident from the centrosymmetry plot in Fig. 3(d) when compared with Fig. 2(c). This process continued until the complete climb of the faulted region by $1d_{111}$ at $\tilde{t} = 3.96 \times 10^4$ ($\equiv$0.14 μs). The schematic diagram in Fig. 4, following Cherns *et al.*,[17] describes the whole process (movie in the Supplementary Material[7]).

Some comments can be made here by comparing our results with the experimental observations of Cherns, Hirsh, and Saka.[17] The evolution of dislocation lines in our case closely matches with the interpretations of their high-temperature results for near-edge dislocations for which they speculated the Thomson-Balluffi mechanism to take place. For pure edge dislocations, however, they considered simultaneous nucleation of loops on both partials, the repulsion between which forces them to climb separately. Since we have allowed for only one "nucleation event," our edge dislocation result, consequently, resembles their near-edge dislocation one.

An NEB simulation was performed in the extended $\{\mathbf{X}_i, \alpha_i, c_i\}$ space to calculate the detailed activation pathway, and the result is shown in Fig. 5(a). The initial configuration as shown in Fig. 2 but without the 3-vacancy roughness was chosen as the node 1. Prior to the NEB calculation, this configuration was allowed to relax by a DMD run during which the system equilibrated with the reservoir, the primary event being concentration equilibration. The other end node was chosen as the configuration right after the extended double jog formation at $\tilde{t} = 1.01 \times 10^4$. Although a lower activation (free) energy of 0.39 eV was found due to the allowance of fractional vacancies, we note that the NEB-generated node 16 is similar to the configuration in Fig. 3(a), indicating that the initial choice of 3-vacancy roughness did not bias the downhill portion of the diffusive-displacive path that the main DMD algorithm captured. Nodes 2, 3, and 4 are translational invariants in energy and were generated due to the end replicas being some distance apart by glide on the {111} plane. In Fig. 5(b), we plot Ω_{DMD} along both mass-action and displacive reaction coordinates, defined respectively as $\Delta M = \sum_{i=1}^{N} c_i - M_0$, M_0 being the total mass of the system at $\tilde{t} = 0$, and $\Delta X = \sqrt{\sum_{i=1}^{N} c_i |\mathbf{X}_i - \mathbf{X}_i^0|^2}$, where $\mathbf{X}_i^0$ is the mean position of site i at $\tilde{t} = 0$. The evolution of Ω_{DMD} shows a downhill process with three distinct regimes. From $\tilde{t} = 0$

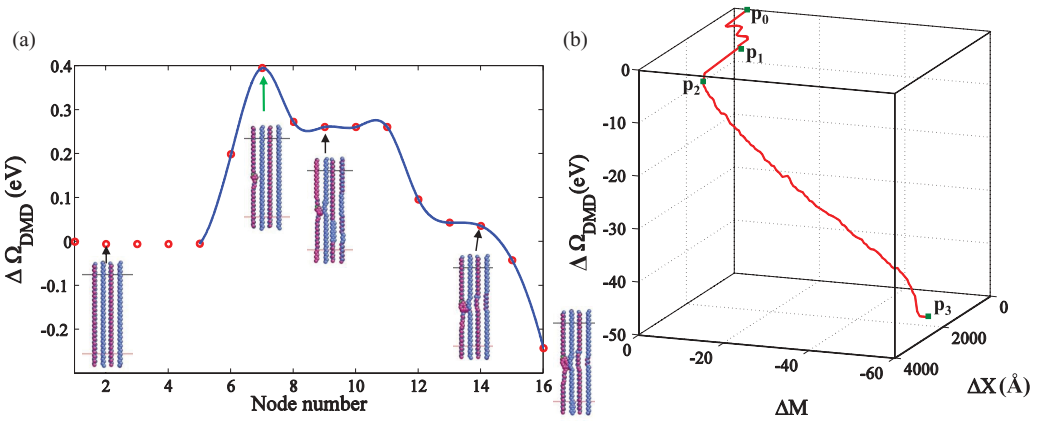

FIG. 5. (Color online) (a) DMD-NEB calculation for the proposed climb pathway showing an activation barrier of 0.39 eV and the corresponding critical nucleus configuration. (b) Grand potential Ω_{DMD} along mass-action and displacive reaction coordinates. Data markers signify four instants: the start p_0 and the end p_3 of the process, and the instants right before (p_1) and after (p_2) the extended double jog formation.

(p_0 in the figure) to the instant right before the extended double jog formation (p_1), diffusive accumulation and displacive movements play equally important roles. However, from p_1 to p_2, the moment when the extended double jog was formed by glide extension, the decrease in Ω_{DMD} is almost entirely due to displacive processes. After p_2 till the end of the process marked by p_3, the evolution is largely dominated by diffusive processes. During this regime, the rate of diffusive accumulation of vacancies, as well as the rate of stress relaxation, was found to be enhanced.[7]

V. CONCLUSION

Though climb of extended edge dislocation has been addressed either by continuum energy calculation or by experiments over the past five decades, an atomistic simulation of the whole process, with detailed atomic configurations and atomic-level energetics, is shown here. Two features of the simulation are noteworthy: (a) A coupled displacive-diffusional pathway emerges out of the DMD simulation automatically, as shown in Fig. 1, and (b) along this pathway, the activation energy of 0.83 eV with $n_C \sim 3$ is lower than the previous theoretical predictions ($\sim 10^1$ eV).[15,16] The minimum energy pathway that the system chose on its own under the prescribed boundary conditions reflects a naturally occurring course that would evolve by a continuous accretion of point defects. It should be mentioned here that even though this pathway is distinctly different from the one proposed by Thomson and Balluffi, the evolution of the dislocation lines agrees overall with the TB mechanism. The usefulness of performing an NEB simulation on the DMD free energy surface should be discussed here. The concept of fractional vacancy brings in an additional degrees of freedom that may allow the NEB method to find an artificially lower activation barrier. Nonetheless, it shows how one can get some quick estimate, albeit a rough one, about the activation path for a system as complex as dislocation dipole. Also, for the present study the NEB method established that the initial choice of 3-vacancy roughness did not bias the downhill portion of the diffusive-displacive path that the main DMD simulation captured. Finally, the real significance of this study is not limited to this particular process, but to stress the importance of "probing" the energy landscape along coupled diffusive-displacive reaction coordinates for the whole class of diffusion-induced defect processes in materials. It demonstrates an ability which has been absent.

ACKNOWLEDGMENTS

The authors acknowledge support by NSF CMMI-0728069. Y.W. also acknowledges support by NSF DMR-1008349 and AFOSR FA9550-09-1-0014. J.L. also acknowledges support by NSF DMR-1008104, DMR-1120901, and AFOSR FA9550-08-1-0325.

*To whom correspondence should be addressed: liju@mit.edu
†To whom correspondence should be addressed: wang.363@osu.edu

[1] Y. Wang and J. Li, Acta Mater. **58**, 1212 (2010).
[2] J. W. Cahn and J. E. Taylor, Acta Mater. **52**, 4887 (2004).
[3] J. P. Hirth and J. Lothe, *Theory of Dislocations* (Krieger Publishing Company, Malabar, FL, 1982), 2nd ed.
[4] F. R. N. Nabarro and F. de Villiers, *Physics of Creep and Creep-Resistant Alloys* (CRC Press, 1995), 1st ed.
[5] O. D. Sherby and P. M. Burke, Prog. Mater. Sci. **13**, 323 (1968).
[6] A. S. Argon and W. C. Moffatt, Acta Metall. **29**, 293 (1981).
[7] See Supplemental Material at http://link.aps.org/supplemental/10.1103/PhysRevB.86.014115 for more discussion and a movie.
[8] J. Li, S. Sarkar, W. T. Cox, T. J. Lenosky, E. Bitzek, and Y. Wang, Phys. Rev. B **84**, 054103 (2011).
[9] R. LeSar, R. Najafabadi, and D. Srolovitz, J. Chem. Phys. **94**, 5090 (1991).
[10] S. R. Phillpot, Phys. Rev. B **49**, 7639 (1994).
[11] A. Stroh, Proc. Phys. Soc. B **67**, 427 (1954).

[12]H. Kimura, R. Maddin, and D. Kuhlmann-Wilsdorf, Acta Metall. **7**, 145 (1959).
[13]R. M. Thomson and R. W. Balluffi, J. Appl. Phys. **33**, 803 (1962).
[14]B. Escaig, Acta Metall. **11**, 595 (1963).
[15]J. Grilhé, M. Boisson, K. Seshan, and R. J. Gaboriaud, Philos. Mag. **36**, 923 (1977).
[16]M. Boisson and R. J. Gaboriaud, Scr. Metall. **14**, 473 (1980).
[17]D. Cherns, P. Hirsch, and H. Saka, Proc. R. Soc. London A **371**, 213 (1980).
[18]C. B. Carter, Philos. Mag. A **41**, 619 (1980).
[19]D. N. Seidman and R. W. Balluffi, Phys. Status Solidi **17**, 531 (1966).
[20]R. W. Balluffi, Phys. Status Solidi **31**, 443 (1969).
[21]R. Pathria, *Statistical Mechanics* (Elsevier Butterworth-Heinemann, 1996), 2nd ed.
[22]S. Phillpot and J. Rickman, J. Chem. Phys. **97**, 2651 (1992).
[23]S. Phillpot, J. Mater. Res. **9**, 582 (1994).
[24]J. Plimpton, J. Comput. Phys. **117**, 1 (1995).
[25]C. Shen, J. Li, and Y. Wang, Metall. Mater. Trans. A **39**, 976 (2008).
[26]G. Henkelman and H. Jónsson, J. Chem. Phys. **113**, 9978 (2000).
[27]G. Henkelman, B. P. Uberuaga, and H. Jónsson, J. Chem. Phys. **113**, 9901 (2000).
[28]H. Jónsson, G. Mills, and K. W. Jacobsen, *Nudged Elastic Band Method for Finding Minimum Energy Paths of Transitions* (World Scientific, Singapore, 1998).
[29]E. Bitzek, P. Koskinen, F. Gähler, M. Moseler, and P. Gumbsch, Phys. Rev. Lett. **97**, 170201 (2006).
[30]Y. Mishin, M. J. Mehl, D. A. Papaconstantopoulos, A. F. Voter, and J. D. Kress, Phys. Rev. B **63**, 224106 (2001).
[31]D. Rodney and G. Martin, Phys. Rev. B **61**, 8714 (2000).
[32]M. Kabir, T. T. Lau, D. Rodney, S. Yip, and K. J. Van Vliet, Phys. Rev. Lett. **105**, 095501 (2010).
[33]G. S. Was, *Fundamentals of Radiation Materials Science: Metals and Alloys* (Springer-Verlag, 2007).
[34]K. Nakashima, M. Suzuki, Y. Futamura, T. Tsuchiyama, and S. Takaki, Mater. Sci. Forum **503-504**, 627 (2006).
[35]M. Militzer, W. P. Sun, and J. J. Jonas, Acta Metall. Mater. **42**, 133 (1994).
[36]T. T. Lau, X. Lin, S. Yip, and K. Van Vliet, Scr. Mater. **60**, 399 (2009).
[37]P. M. Hazzledine, H. P. Karnthaler, and E. Wintner, Philos. Mag. **32**, 81 (1975).